Dynamic in-situ sensing of fluid-dispersed 2D materials integrated on microfluidic Si chip

Benjamin T. Hogan[†,‡], Sergey A. Dyakov[§], Lorcan J. Brennan[#], Salma Younesy[†,%], Tatiana S. Perova[§,√], Yurii K. Gun'ko[#,√], Monica F. Craciun[†] and Anna Baldycheva[*,†,$]

[†] Department of Engineering and Centre for Graphene Science, College of Engineering, Mathematics and Physical Sciences, University of Exeter, Exeter, EX4 4QF, UK.

[‡] EPSRC Centre for Doctoral Training in Electromagnetic Metamaterials, University of Exeter, EX4 4QL, UK.

[§] Skolkovo Institute of Science and Technology, Photonics and Quantum Material Centre, Nobel Street 3, Moscow, Russia.

[#] School of Chemistry and CRANN, University of Dublin, Trinity College, Dublin 2, Ireland.

[%] École Nationale Supérieure de Mécanique et des Microtechniques, Besançon, France.

[$] Department of Electronic and Electrical Engineering, University of Dublin, Trinity College, Dublin 2, Ireland.

[√] ITMO University, 49 Kronverskiy pr., St.-Petersburg, 197101, Russia.

In this work, we propose a novel approach for wafer-scale integration of 2D materials on CMOS photonics chip utilising methods of synthetic chemistry and microfluidics technology. We have successfully demonstrated that this approach can be used for integration of any fluid-dispersed 2D nano-objects on silicon-on-insulator photonics platform. We demonstrate for the first time that the design of an optofluidic waveguide system can be optimised to enable simultaneous *in-situ* Raman spectroscopy monitoring of 2D dispersed flakes during the device operation. Moreover, for the first time, we have successfully demonstrated the possibility of label-free 2D flake detection via selective enhancement of the Stokes Raman signal at specific wavelengths. We discovered an ultra-high signal sensitivity to the xyz alignment of 2D flakes within the optofluidic waveguide, which in turn enables precise *in-situ* alignment detection for the first practicable realisation of 3D photonic microstructure shaping based on 2D-fluid composites and CMOS photonics platform while also representing a useful technological tool for the control of liquid phase deposition of 2D materials.

The recent development of nanocomposites consisting of fluid-dispersed atomically thin two-dimensional (2D) materials has sparked a great level of interest as a highly promising *in-situ* tailored meta-material device platform for the next generation of multi-functional optoelectronic systems[1–13]. Dynamically controlled three-dimensional (3D) self-assembly of fluid-suspended 2D materials not only provides a new breakthrough route for technological applications of 2D material based 3D device architectures[14–16], but also their fluidic nature allows CMOS-compatible wafer-scale back-end integration on chip using microfluidic technology[17–19]. The practical realisation of dynamically reconfigurable 3D material fluid metastructures integrated into a microfluidic system and coupled with a CMOS photonic circuit (as illustrated in Fig. 1)

2

opens up limitless possibilities in the fabrication of compact and low-power systems for 40

commercially viable, miniaturised, multi-functional light-management devices such as light 41

emitting sources[20], tuneable optical filters[21] and nanoantenna phased arrays[22]. For example, 1D 42

photonic crystals of graphene which could act as optical filters have been theoretically explored[23] 43

but as yet no method exists for the precise reconfigurable control of such structures. 44

Additionally, self-assembly of fluid dispersed 2D materials represents a remarkable precursor 45

state for liquid phase deposition of ordered lamellae, stacks and other structures in the solid 46

phase[24–26]. Reconfigurability of the metastructures can be achieved by exploiting liquid crystal 47

technology[6,15] with in-situ monitoring used to characterise the metastructure formation. 48

However, the primary challenge for the first realisation of on-chip controlled assembly of 2D 49

flakes into functional metastructures is the lack of a reliable and sensitive method for *in-situ* 50

characterisation. Such a method is pivotal to the confirmation of the integration of composites in 51

the device and to enable determination of parameters, such as spatial alignment of incorporated 52

2D materials, dynamically during device operation. Conventional characterisation methods such 53

as Raman spectroscopy[5,27,28], coherent anti-Stokes Raman spectroscopy (CARS)[29] and Fourier 54

Transform Infrared Spectroscopy (FTIR)[30] are not suitable for studies of fluid nanocomposites 55

with relatively low concentrations of nanoparticles dispersed. In this case, the significantly 56

greater scattering volume of the host fluid compared to that of the dispersed nanoparticles always 57

dominates the vibrational signal intensity, rendering the monitoring of the considerably weaker 58

bands of dispersed nanoparticles impossible. 59

Here we demonstrate, for the first time, the wafer-scale integration of fluid-dispersed 2D 60

materials on Si photonics chip utilising microfluidic technology, and their subsequent electrical 61

and optical manipulation. We also propose and subsequently demonstrate a novel approach for 62

ultra-sensitive, label-free, *in-situ* detection and monitoring of integrated 2D-fluid composite 63

materials on-chip. Specifically, an *in-situ* micro-Raman characterisation approach, whereby the 64

Raman signal of 2D dispersed nanoparticles is selectively enhanced through the design of 65

optofluidic waveguide geometry on silicon-on-insulator (SOI) platform. It has previously been 66

shown that the Raman signal from micro-structured silicon cavities can be enhanced due to 67

Fabry-Pérot type resonances[31–33]. Here, the structure is designed to simultaneously enhance 68

different resonant modes relating to different parameters of the optofluidic waveguides, 69

balancing the required enhancement of the signal from multiple vibrational bands with the desire 70

for the greatest achievable intensity for the individual bands. The developed approach 71

demonstrates ultra-high sensitivity to the xyz alignment of 2D nanoparticles within optofluidic 72

waveguides. Hence, for the first time, our findings demonstrate the possibility of monitoring the 73

dynamics of fluid-dispersed 2D nanoparticles on chip. Our work paves the way for the 74

practical realisation of dynamically reconfigurable photonic metastructures based on 2D-fluid 75

composites integrated on CMOS photonics platform with a range of important applications, such 76

as renewable energy, optical communications, bio-chemical sensing, and security and 77

defence technologies[4,8,34] or as a precursor to controlled deposition of solid state structures[24–26]. 78

79

Typically, large-scale CMOS photonics builds on a SOI platform; a high index-contrast 80

waveguide platform which prevents interference between the photonic integrated circuit 81

components and the substrate. Therefore, we use an SOI based Fabry-Pérot type optofluidic 82

waveguide channel, with an open top cladding (Fig. 1 inset) to allow *in-situ* micro-Raman 83

detection and monitoring of the integrated 2D fluid nanocomposite system during device 84

operation. To optimise the optofluidic waveguide design for facilitating strong confinement of 85

4

light on chip and to significantly enhance the Raman back-scattered signal of the individual 86

incorporated 2D nanoplatelets, we model the variation in the intensity of the Raman bands of 87

dispersed nanoparticles while varying parameters that can be experimentally controlled, such as: 88

the waveguide width, w, and the buffer oxide (BOX) layer thickness, h_{BOX}. We consider the 89

specific case of the D and G bands of 2D carbon-based materials (Fig. 2)- such as graphene and 90

graphene oxide (GO)- dispersed in a nematic liquid crystal (LC) host, however the proposed 91

methodology can be utilised for any fluid-dispersed material. The backscattered Raman signal 92

intensity is numerically determined for wavelengths corresponding to the Raman active bands 93

using the scattering matrix method [See Supplementary Methods]. The complex variation of the 94

Raman signal as a result of modifying the optofluidic waveguide parameters can be rationalised 95

as the superposition of Fabry-Pérot resonance effects in different parts of the geometry. 96

Enhancement of up to 100x can be observed between maximising and minimising combinations 97

of the optofluidic waveguide parameters. 98

In order to experimentally demonstrate the enhancement of the Raman intensity, 2D material- 99

fluid nanocomposites- consisting of graphene and GO nanoplatelets dispersed in LCs- were 100

prepared by a liquid phase dispersion method [See Supplementary Methods]. The optimal 101

parameters for the microfluidic structures were determined from the calculated Raman signal 102

intensity maps shown in Figure 2. Resonator devices consisting of optofluidic waveguide 103

channels of different widths were fabricated on SOI wafer with a thick buffer oxide (h_{BOX}=2 μm) 104

layer and with a silicon device layer of 15 μm. The prepared nanocomposites were integrated 105

into optofluidic waveguide channels via infiltration reservoirs on the chip (Fig. 3). The selected 106

microfluidic channels had widths in the ranges 3.7±0.2 μm (narrow channels, strong 107

enhancement) and 10.5±1.5 μm (wide channels, weaker enhancement). Optical microscopy (Fig. 108

3b) and scanning electron microscopy (Fig. 3c-e) both confirmed the successful integration of 109

the nanocomposite into all channels. 110

Raman spectra are presented for the GO-LC nanocomposites- with MLC-6608 (Fig. 4a) and 111

with E7 (Fig. 4b) as the fluid host- at three points *in-situ* on the chip; more specifically: in a wide 112

channel (Fig. 4c), in a narrow channel (Fig. 4d) and in an infiltration reservoir (Fig. 4e). Liquid 113

crystal MLC-6608 exhibits weak Raman bands (see Supplementary Results) that have no strong 114

overlap with the D and G bands, allowing for clear determination of the GO bands in gathered 115

spectra. Raman spectra were recorded for individual monolayer flakes of area 1.0 ± 0.1 μm^2 in all 116

cases. For GO dispersed in MLC-6608, the D band Raman intensities were observed in the 117

approximate ratio 5:8:16 for an infiltration reservoir, 11.6 μm channel and 3.6 μm channel 118

respectively. For the G band, intensities were observed in the ratio 5:7:16. E7, however, has a 119

strong Raman active vibrational band at around 1605 cm^{-1} (see Supplementary Results), 120

overlapping with the G band. Nevertheless, utilising the proposed signal enhancing design, the 121

observation of the G band as a broad shoulder on this band is feasible (Fig. 4b). In addition, 122

similar results were obtained for nanocomposites with graphene instead of GO. 123

The close agreement, in Figure 4f, between the relative intensities of the D and G bands found 124

experimentally for all nanocomposites (points) and those determined numerically (solid lines) 125

verifies the method for predicting the Raman signal enhancement. For both the D and G bands, 126

the numerically determined enhancement ratio was within the error of the experimental 127

measurements; slight differences occur due to the flake not being positioned precisely at the 128

centre of the channel. Therefore, this technique presents an effective tool for maximising the 129

enhancement of the Raman signal. 130

Understanding the dynamics of 2D nanoplatelet spatial alignment is essential for the realisation of three-dimensional metastructure formation. External stimuli, such as applied electric field and light coupling[6,15] [See Supplementary Results and Supplementary Videos 1-4], induce dynamic re-ordering of suspended 2D nanoparticles. Here, a Raman laser was exploited to move a GO flake within a channel (Fig. 5a), while simultaneously being used to monitor the xyz alignment over time. The variation in the experimental Raman spectra for different flake positions within the channel is illustrated in Fig 5b.

The effect of the flake position on the Raman signal intensity was modelled by varying the position of the oscillating dipoles within the optofluidic waveguide channel both laterally and vertically. The ratio of the D and G band intensities is not constant as the position is varied (Fig. 5c-d). For lateral displacements (Fig. 5c), there are ratios of 11 and 32 between the minimal and maximal intensities determined numerically for the D and G bands respectively. For vertical displacements (Fig. 5d), the maximum and minimum values of the average intensity differ by factors of around four and five times for the D and G bands respectively.

For the lateral displacement of the flake, the ratios of the intensities of the GO D and G bands were extracted from experimental spectra when a flake was next to the wall and when moved further towards the centre of the channel. These ratios were then used as a multiplier on the numerically determined intensity for the flake next to the wall (position 2 in Fig. 5a) to determine an approximate displacement. Positions approximated using experimental data in tandem with the numerically determined results are closely matched to the values observed using optical microscopy techniques (See Supplementary Results), falling within the experimental error. The lateral position can therefore be determined with similar precision to optical

131
132
133
134
135
136
137
138
139
140
141
142
143
144
145
146
147
148
149
150
151
152

microscopy (approx. ±5%) currently, but with scope for the error to be reduced significantly by   153

improving the signal-to-noise ratio.   154

For the vertical displacement of the flake, again the ratios of the intensities of the GO D and G   155

bands were extracted, this time from data with the flake at the bottom of the channel and further   156

towards the surface. The ratios were then used to multiply the numerically determined intensity   157

with the flake at the bottom of the channel to determine an approximate displacement. The   158

numerical analysis covering the effect of vertical flake position shows close agreement with the   159

experimental data. The vertical position of the flake cannot be determined from optical   160

microscopy but the close agreement of the positions determined separately from the D and G   161

bands confirms that the method is accurate. Therefore, the predictions made from the Raman   162

spectra are the most accurate method of determining the vertical position currently available.   163

While we propose this technique as a method for monitoring self-assembly of 3D metastructures   164

comprised of 2D materials, this approach may also find applications in a wide range of other   165

areas such as controlling flake alignment for liquid phase deposition of 2D materials[24,26] or for   166

spatial monitoring of nanoparticle distributions[35].   167

In summary, we propose a novel approach for integration of 2D materials on CMOS photonics   168

chip utilising microfluidics technology. We have successfully demonstrated that this approach   169

can be used for integration of any fluid-dispersed 2D nanoparticles on SOI photonics platform.   170

The optofluidic system design can be optimised to enable *in-situ* Raman spectroscopy   171

monitoring of 2D dispersed flakes during device operation. *In-situ* label-free 2D flake sensing   172

via selective enhancement of the Stokes Raman signal at given wavelengths has been determined   173

numerically and confirmed experimentally. This approach has been applied to monitor the   174

individual 2D nanoplatelet dynamic within an optofluidic waveguide with high sensitivity,   175

enabling precise *in-situ* alignment monitoring for controlling liquid phase deposition of 2D materials as well asthe first practical realisation of 3D photonic metastructure shaping based on 2D-fluid composites and CMOS photonics platform.

ASSOCIATED CONTENT

Supporting Information

ACKNOWLEDGMENTS

AUTHOR INFORMATION

Corresponding Author

*Email: a.baldycheva@exeter.ac.uk 198

Author Contributions 199

A.B. conceived and planned the research, analysed data. A.B and B.H. wrote the paper with 200

input from M.C., T.P., Y.G..; A.B., T.P., B.H. and S.Y. conducted the experiments; S.D. wrote 201

the code used for numerical analysis; L.B. synthesised the nanocomposites; A.B. and M.C. 202

supervised and directed the research. All authors read and approved the final manuscript. 203

ADDITIONAL INFORMATION 204

Competing Financial Interests 205

REFERENCES 207

1. Behabtu, N. *et al.* Spontaneous high-concentration dispersions and liquid crystals of 208
    graphene. *Nat. Nanotechnol.* **5,** 406–11 (2010). 209

2. Engel, M. *et al.* Light–matter interaction in a microcavity-controlled graphene transistor. 210
    Nat. Commun. **3,** 906 (2012). 211

3. Bao, Q. & Loh, K. P. Graphene Photonics, Plasmonics, and Broadband Optoelectronic 212
    Devices. *ACS Nano* **6,** 3677–3694 (2012). 213

4. Xia, F., Wang, H., Xiao, D., Dubey, M. & Ramasubramaniam, A. Two-dimensional 214
    material nanophotonics. *Nat. Photonics* **8,** 899–907 (2014). 215

5. Ferrari, A. C. *et al.* Raman Spectrum of Graphene and Graphene Layers. *Phys. Rev. Lett.* 216
    97, 187401 (2006). 217

6. Shen, T.-Z., Hong, S.-H. & Song, J.-K. Electro-optical switching of graphene oxide liquid 218
    crystals with an extremely large Kerr coefficient. *Nat. Mater.* **13,** 394–9 (2014). 219

7.   Zakri, C. *et al.* Liquid crystals of carbon nanotubes and graphene. *Philos. Trans. R. Soc. A Math. Phys. Eng. Sci.* **371,** 20120499 (2013).

8.   Ferrari, A. C. *et al.* Science and technology roadmap for graphene, related two-dimensional crystals, and hybrid systems. *Nanoscale* **7,** 4598–4810 (2015).

9.   Li, S. *et al.* Enhanced photorefractive and third-order nonlinear optical properties of 5CB-based polymer-dispersed liquid crystals by graphene doping. *J. Phys. Chem. C* **118,** 18015–18020 (2014).

10.   Khan, A. A. *et al.* Graphene and chiral nematic liquid crystals: a focus on lasing. *RSC Adv.* **5,** 57437–57443 (2015).

11.   Akbari, A. *et al.* Large-area graphene-based nanofiltration membranes by shear alignment of discotic nematic liquid crystals of graphene oxide. *Nat. Commun.* **7,** 10891 (2016).

12.   Yu, L., Cheng, Z., Dong, Z., Zhang, Y. & Yu, H. Photomechanical response of polymer-dispersed liquid crystals/graphene oxide nanocomposites. *J. Mater. Chem. C* **2,** 8501–8506 (2014).

13.   Shivanandareddy, A. B., Krishnamurthy, S., Lakshminarayanan, V. & Kumar, S. Mutually ordered self-assembly of discotic liquid crystal-graphene nanocomposites. *Chem. Commun. (Camb).* **50,** 710–2 (2014).

14.   He, L. *et al.* Graphene oxide liquid crystals for reflective displays without polarizing optics. *Nanoscale* **7,** 1616–22 (2015).

15.   Tie, W. *et al.* Dynamic electro-optic response of graphene/graphitic flakes in nematic liquid crystals. *Opt. Express* **21,** 19867–79 (2013).

16.   Islam, M. M. *et al.* Liquid Crystalline Graphene Oxide/PEDOT:PSS Self-Assembled 3D Architecture for Binder-Free Supercapacitor Electrodes. *Front. Energy Res.* **2,** (2014).

17. Li, Q. *Nanoscience with Liquid Crystals*. (Springer International Publishing, 2014). 243
doi:10.1007/978-3-319-04867-3 244

18. Soltani, M., Inman, J. T., Lipson, M. & Wang, M. D. Electro-optofluidics: achieving 245
dynamic control on-chip. *Opt. Express* **20,** 22314–26 (2012). 246

19. Huang, Y. & Mason, A. J. Lab-on-CMOS integration of microfluidics and electrochemical 247
sensors. *Lab Chip* **13,** 3929–34 (2013). 248

20. Coles, H. & Morris, S. Liquid-crystal lasers. *Nat. Photonics* **4,** 676–685 (2010). 249

21. Caputo, R. *et al.* POLICRYPS: a liquid crystal composed nano/microstructure with a wide 250
range of optical and electro-optical applications. *J. Opt. A Pure Appl. Opt.* **11,** 24017 251
(2009). 252

22. Ni, X., Emani, N. K., Kildishev, A. V, Boltasseva, A. & Shalaev, V. M. Broadband Light 253
Bending with Plasmonic Nanoantennas. *Science (80-.).* **335,** 427–427 (2012). 254

23. Fan, Y., Wei, Z., Li, H., Chen, H. & Soukoulis, C. M. Photonic band gap of a graphene- 255
embedded quarter-wave stack. *Phys. Rev. B - Condens. Matter Mater. Phys.* **88,** 241403 256
(2013). 257

24. Jalili, R. *et al.* Processable 2D materials beyond graphene: MoS 2 liquid crystals and 258
fibres. *Nanoscale* **8,** 16862–16867 (2016). 259

25. Jalili, R. *et al.* Scalable One-Step Wet-Spinning of Graphene Fibers and Yarns from 260
Liquid Crystalline Dispersions of Graphene Oxide: Towards Multifunctional Textiles. 261
Adv. Funct. Mater. **23,** 5345–5354 (2013). 262

26. Jalili, R. *et al.* Organic Solvent-Based Graphene Oxide Liquid Crystals: A Facile Route 263
toward the Next Generation of Self-Assembled Layer-by-Layer Multifunctional 3D 264
Architectures. *ACS Nano* **7,** 3981–3990 (2013). 265

27. Castriota, M. *et al.* In situ polarized micro-Raman investigation of periodic structures realized in liquid-crystalline composite materials. *Opt. Express* **19,** 10494 (2011).

28. Guddala, S., Dwivedi, V. K., Vijaya Prakash, G. & Narayana Rao, D. Raman scattering enhancement in photon-plasmon resonance mediated metal-dielectric microcavity. *J. Appl. Phys.* **114,** 224309 (2013).

29. Zheltikov, A. M. Nano-optical dimension of coherent anti-Stokes Raman scattering. *Laser Phys. Lett.* **1,** 468–472 (2004).

30. Xu, J., Wang, K., Zu, S.-Z., Han, B.-H. & Wei, Z. Hierarchical Nanocomposites of Polyaniline Nanowire Arrays on Graphene Oxide Sheets with Synergistic Effect for Energy Storage. *ACS Nano* **4,** 5019–5026 (2010).

31. Kuzik, L. A., Yakovlev, V. A. & Mattei, G. Raman scattering enhancement in porous silicon microcavity. *Appl. Phys. Lett.* **75,** 1830 (1999).

32. Mamichev, D. A. *et al.* Enhanced Raman scattering in multilayer structures of porous silicon. *J. Raman Spectrosc.* **42,** 1392–1395 (2011).

33. Mamichev, D. A. *et al.* Enhanced Raman scattering in grooved silicon matrix. *Phys. status solidi* **246,** 173–176 (2009).

34. Hui Chen, Z., Long Tan, Q., Lao, J., Liang, Y. & Guang Huang, X. Reconfigurable and tunable flat graphene photonic crystal circuits. *Nanoscale* **7,** 10912–10917 (2015).

35. Mezzenga, R. & Ruokolainen, J. Nanocomposites: Nanoparticles in the right place. *Nat. Mater.* **8,** 926–928 (2009).

266
267
268
269
270
271
272
273
274
275
276
277
278
279
280
281
282
283
284
285

286

Figure 1. A CMOS photonic circuit coupled to a microfluidic layer integrating dynamically reconfigurable 2D material metastructures by exploiting liquid crystal technology. *In-situ* micro-spectroscopy detection and monitoring gives information on the formation of the metastructures.

287

Figure 2. a) Map showing regions where both the D and G bands of 2D carbon-based materials are determined numerically to be strongly enhanced in Raman spectroscopy measurements. **b**) Expanded view of the region of interest highlighted in a. The range of parameters for which strong enhancement is observed are shown with the white lines including fabrication deviation Δh_{BOX} and Δw.

288

Figure 3. a) SEM image of the chip used for Raman measurements, before infiltration with the nanocomposite. **b**) Polarised microscopy image of the structure infiltrated with a composite of MLC 6608 and graphene oxide. Integration of the composite, including GO flakes, into all microfluidic structures on the chip can be seen. **c**) SEM of GO flakes infiltrated with a host LC into a 3.6 μm channel. **d**) SEM of GO flakes infiltrated with a host LC into an 11.6 μm channel. **e**) SEM of an 11.6 μm channel, with the LC removed, showing the integration of large numbers of GO flakes.
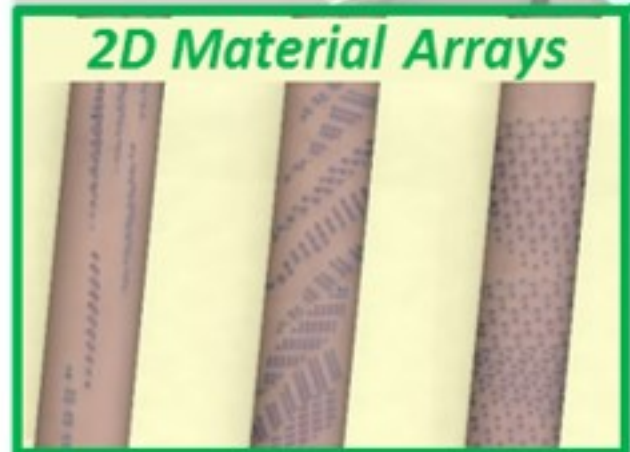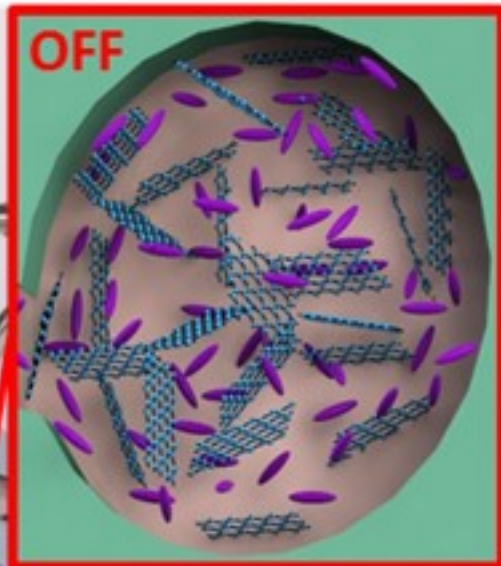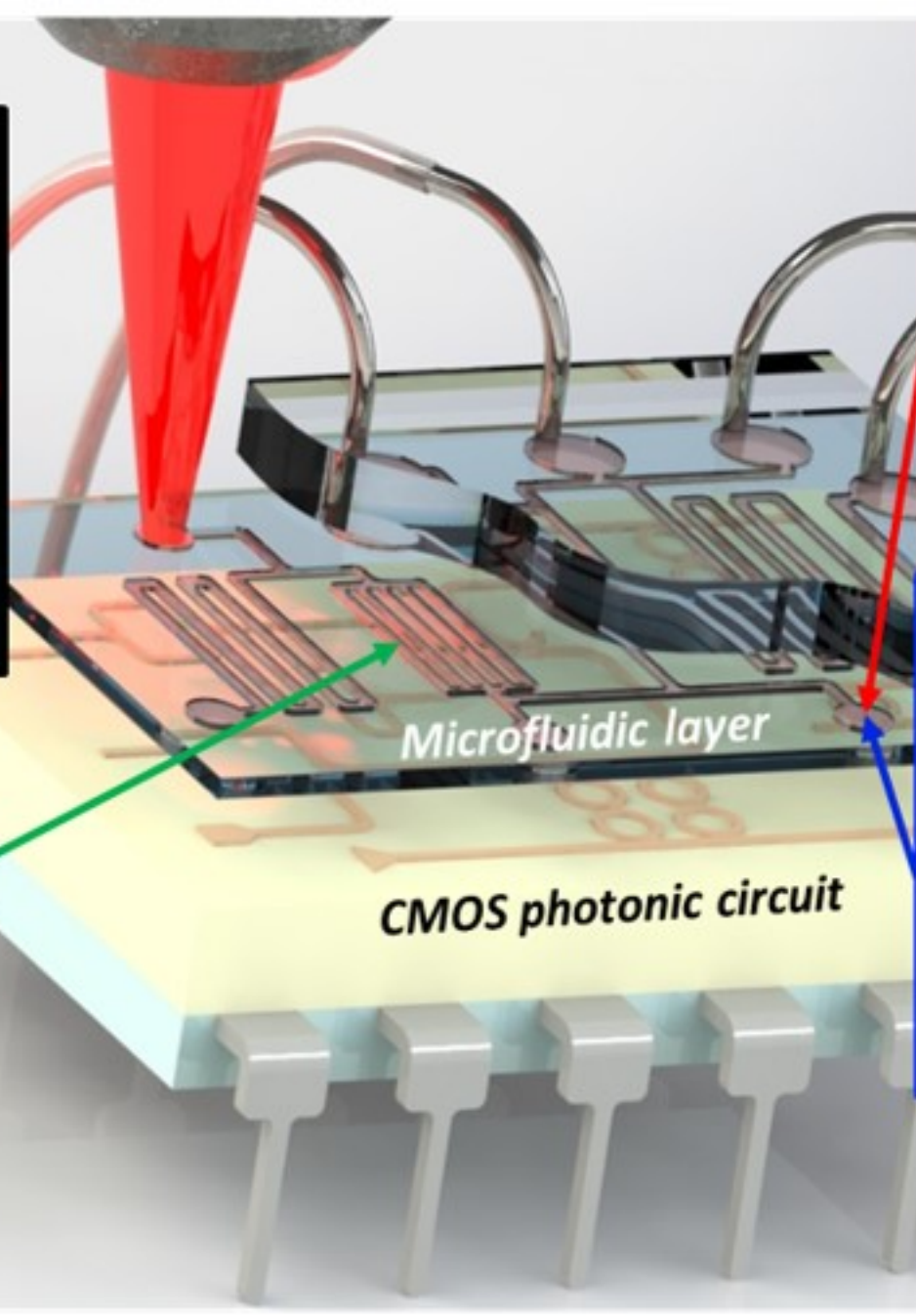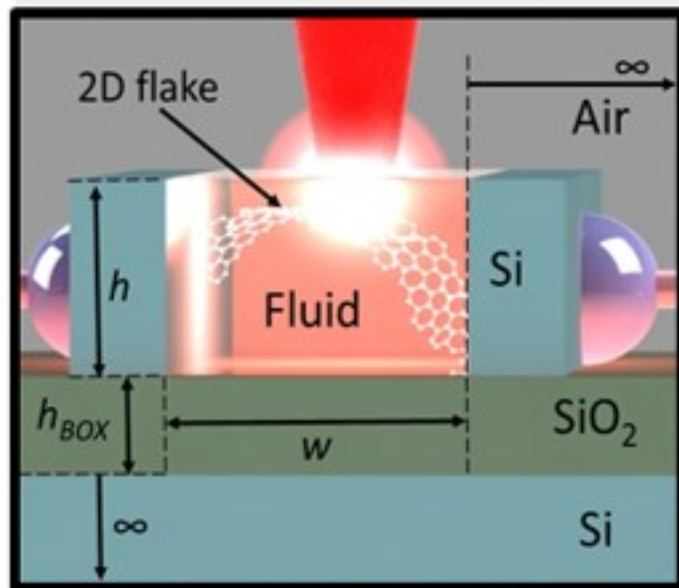
Figure 4. a-b) Normalized Raman spectra showing the enhancement of the D and G bands for graphene oxide dispersed in (**a**) liquid crystal MLC 6608 and (**b**) liquid crystal E7. Spectra are shown for three microfluidic geometries: in (**c**) an infiltration reservoir of width 100μm (magenta), in (**d**) a microfluidic cavity of width 11.6μm (green) and in (**e**) a microfluidic cavity of width 3.6μm (black). Approximate laser spot sizes are shown in (**c-e**). **f**) Comparison of numerically determined (solid lines) and experimentally measured (points) Raman intensities of the graphene oxide D (blue) and G (red) bands. All data is normalized to the case where the walls are separated by a distance great enough for Fabry-Pérot resonances to have no effect.
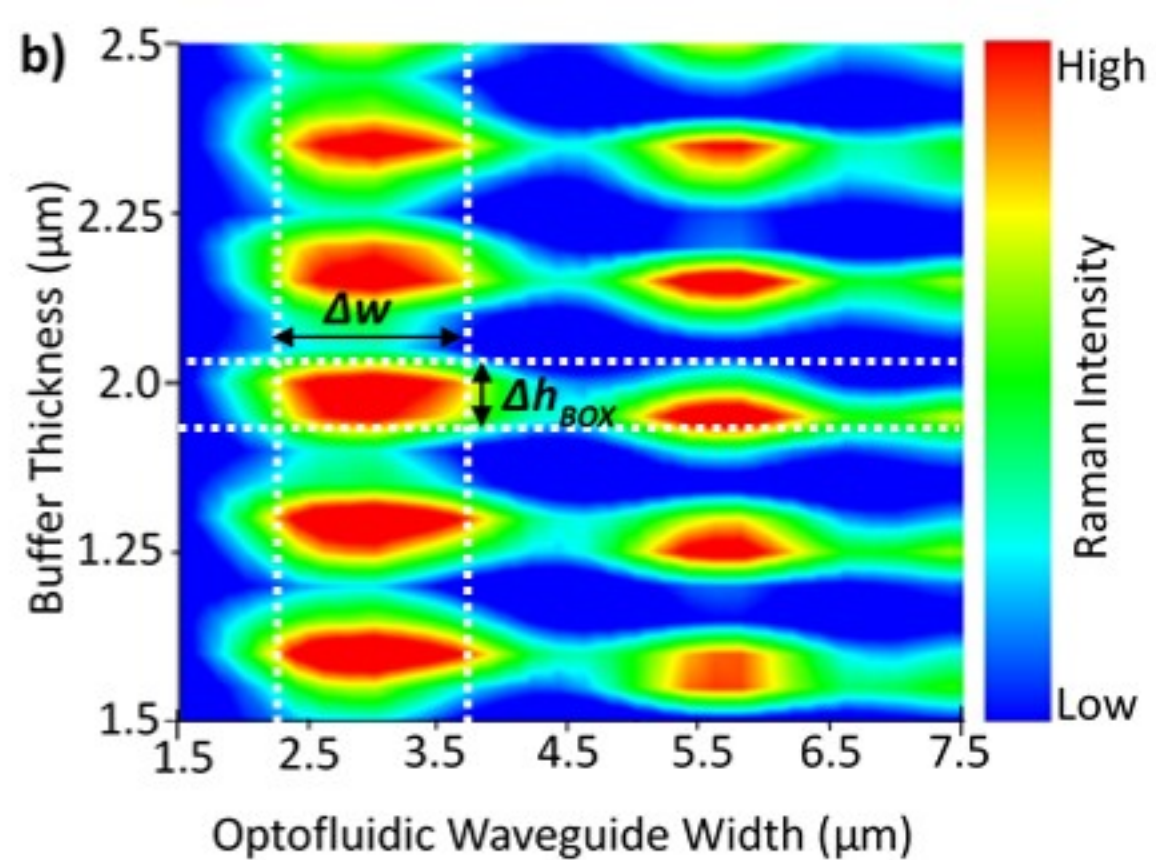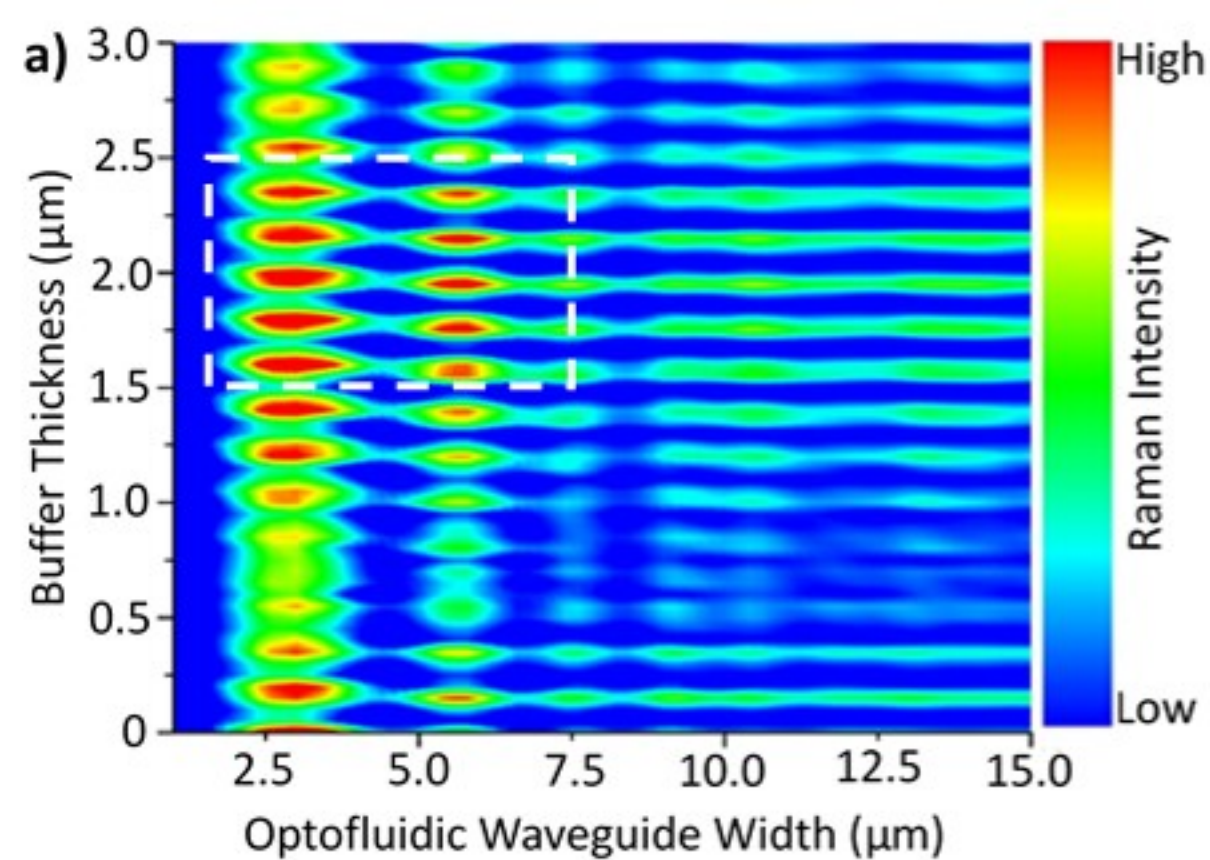
289

290

Figure 5. a) GO flake movement induced by the Raman laser. Each image represents the change after 10 *s* exposure time in the order in which they were observed. **b**) Raman spectra of a GO flake dispersed in liquid crystal E7 within a narrow channel (approx. 3.6 *μm*) at positions 1 (cyan), 2 (violet) and 5 (grey) as seen in **a**. **c-d**) The variation of the Raman intensity of the GO D (blue) and G (red) bands for lateral (**c**) and vertical (**d**) displacements of a GO flake within the microfluidic channel. Solid lines give the numerically determined Raman intensities. Flake positions determined from normalized experimental spectra are shown as points. For lateral displacements, the error in the experimental measurement is given by the size of the symbols.
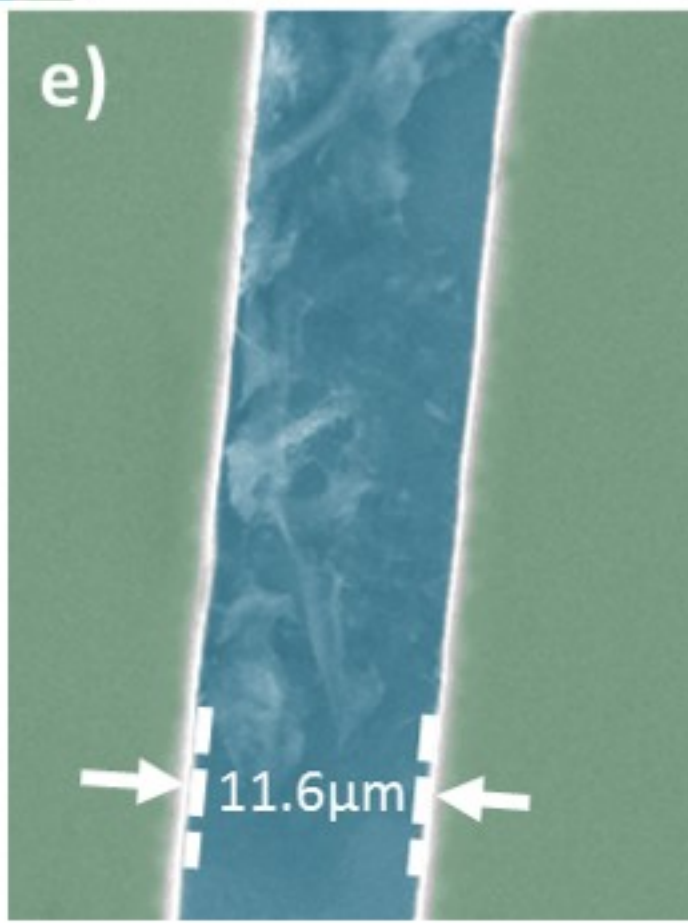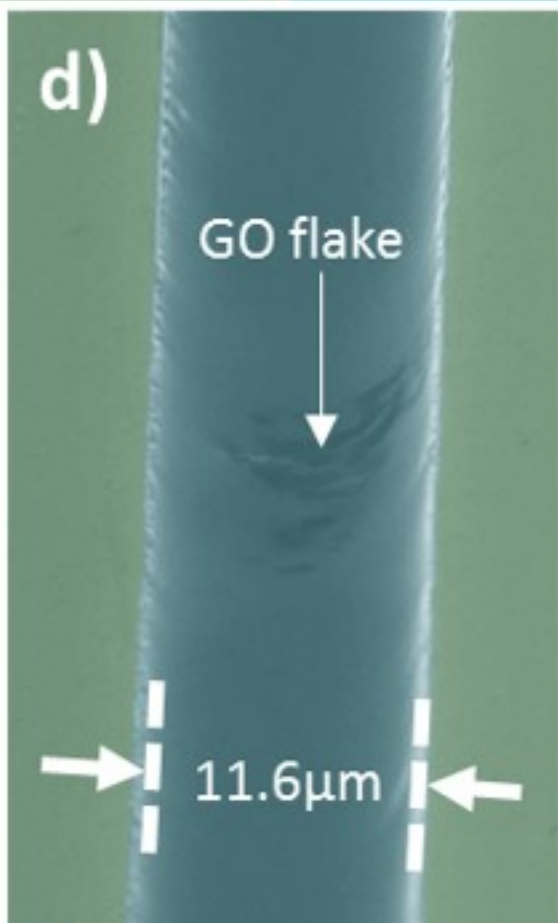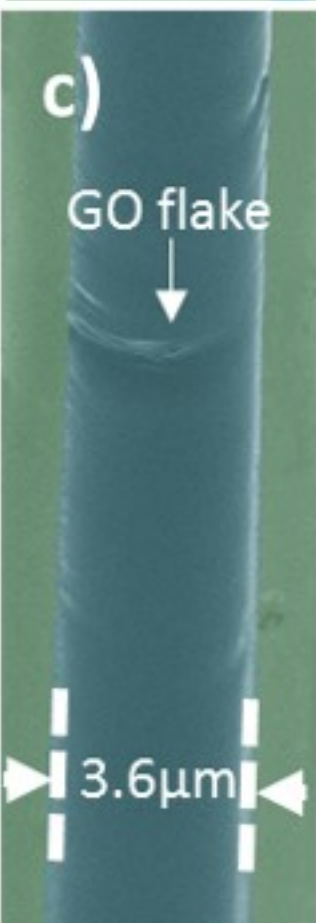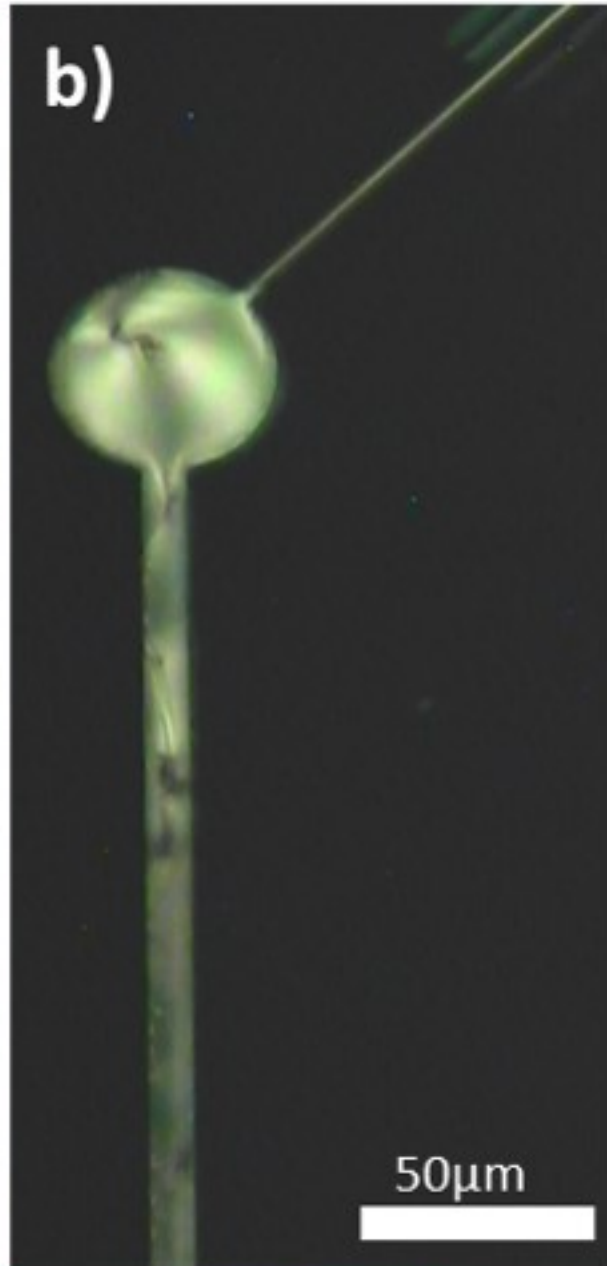
In-situ monitoring

2D flake

Air

∞

h

Fluid

Si

h_{BOX}

w

SiO$_2$

∞

Si

OFF

ON

Microfluidic layer

CMOS photonic circuit

2D Material Arrays
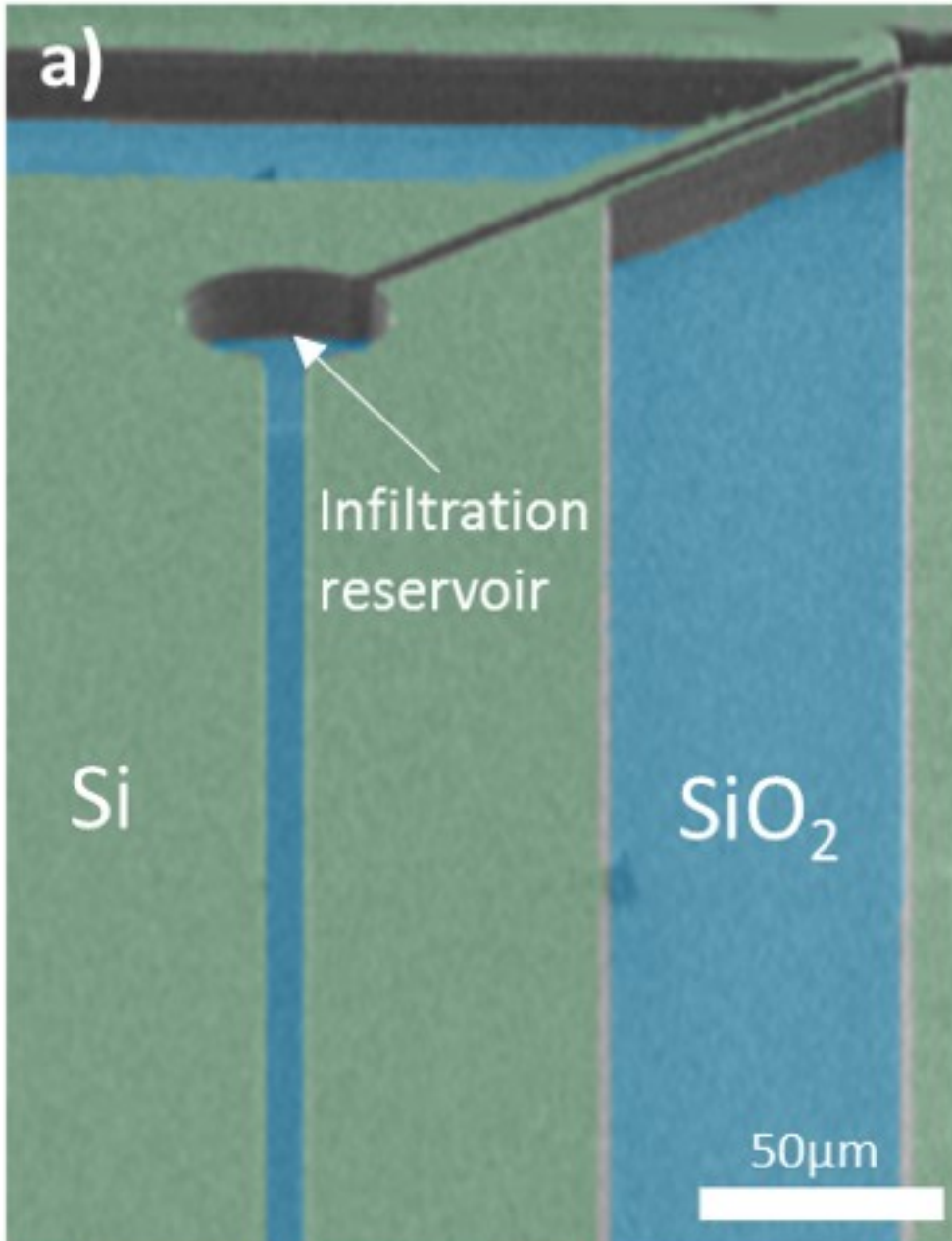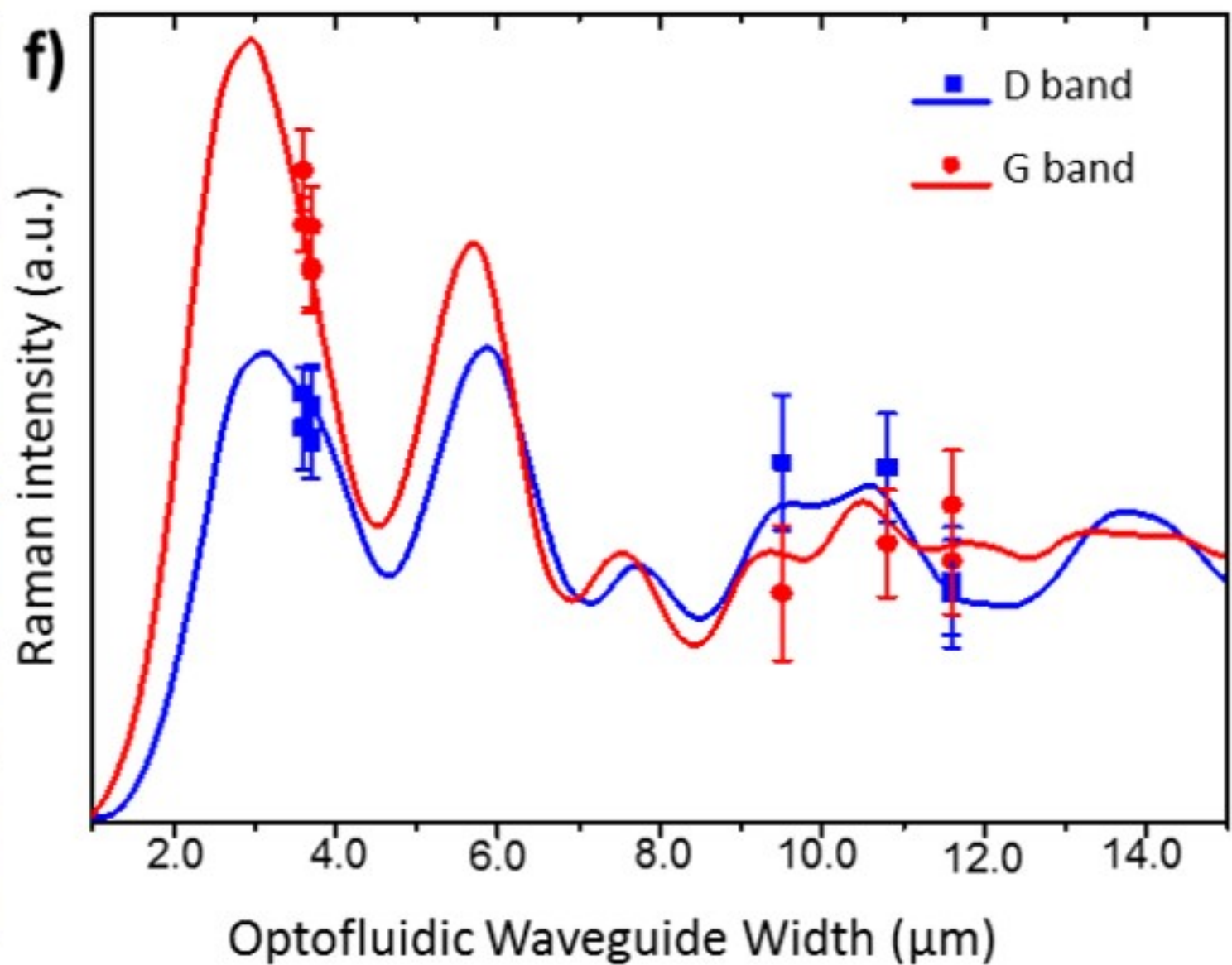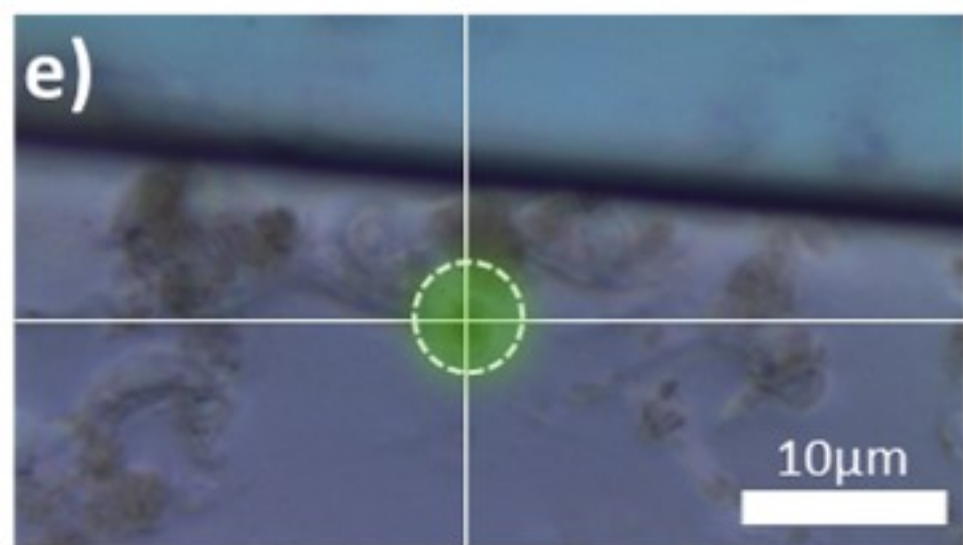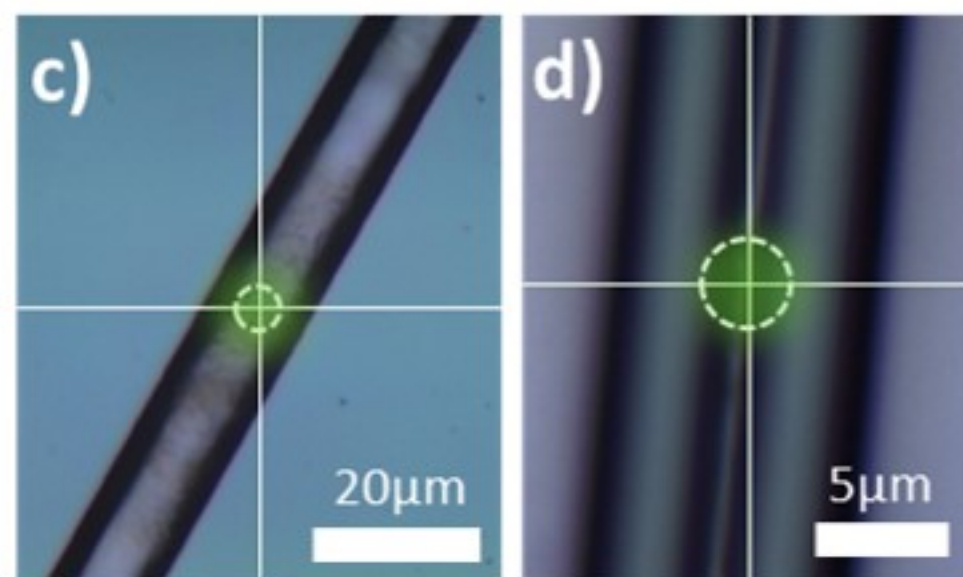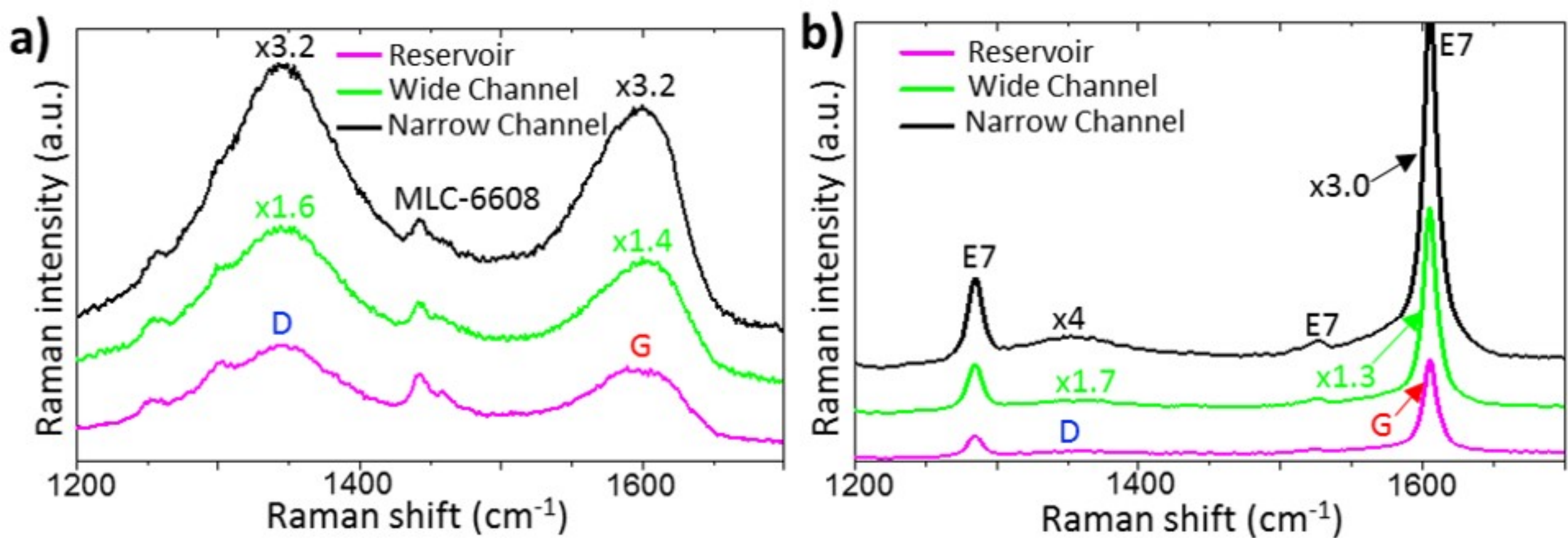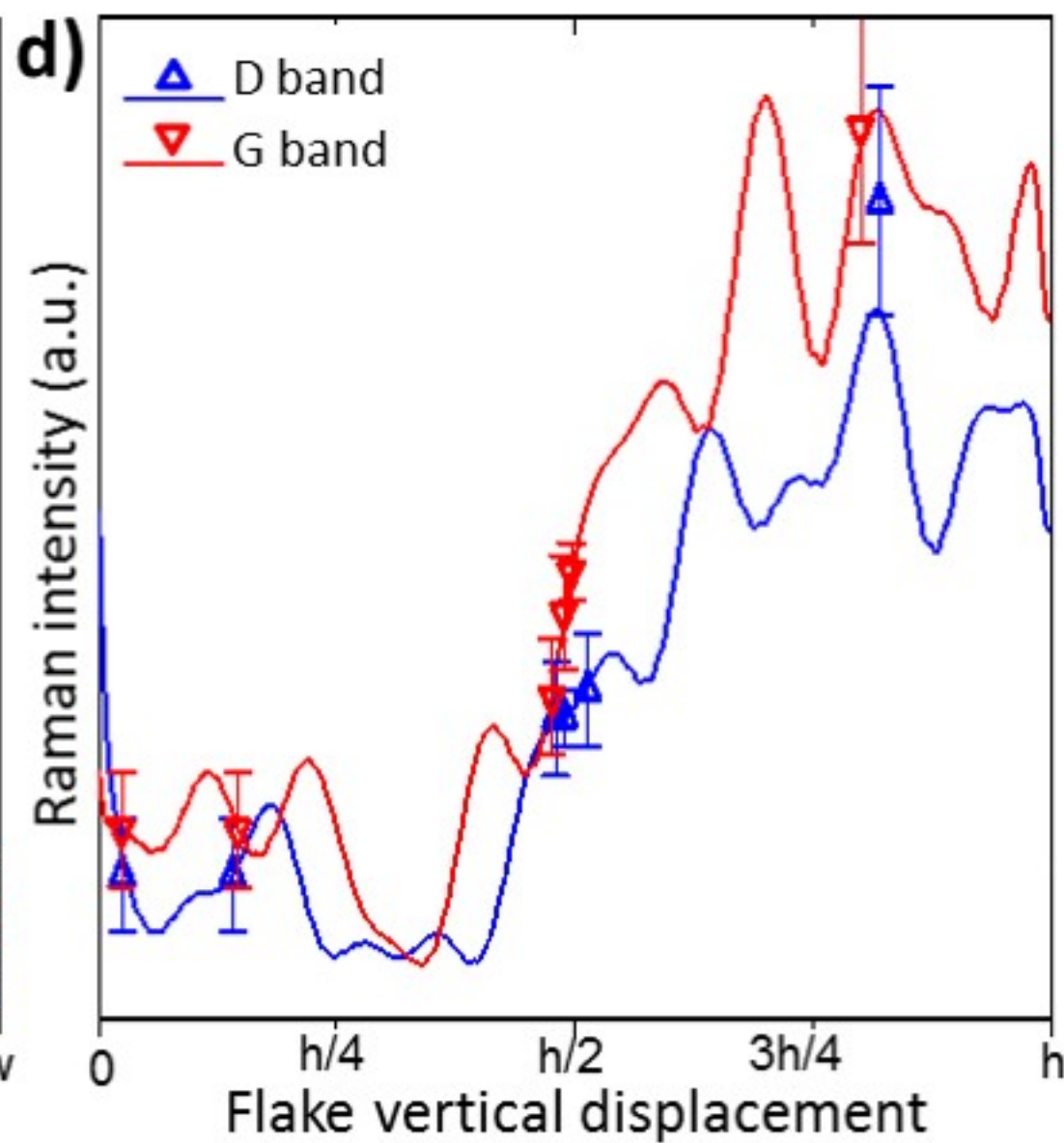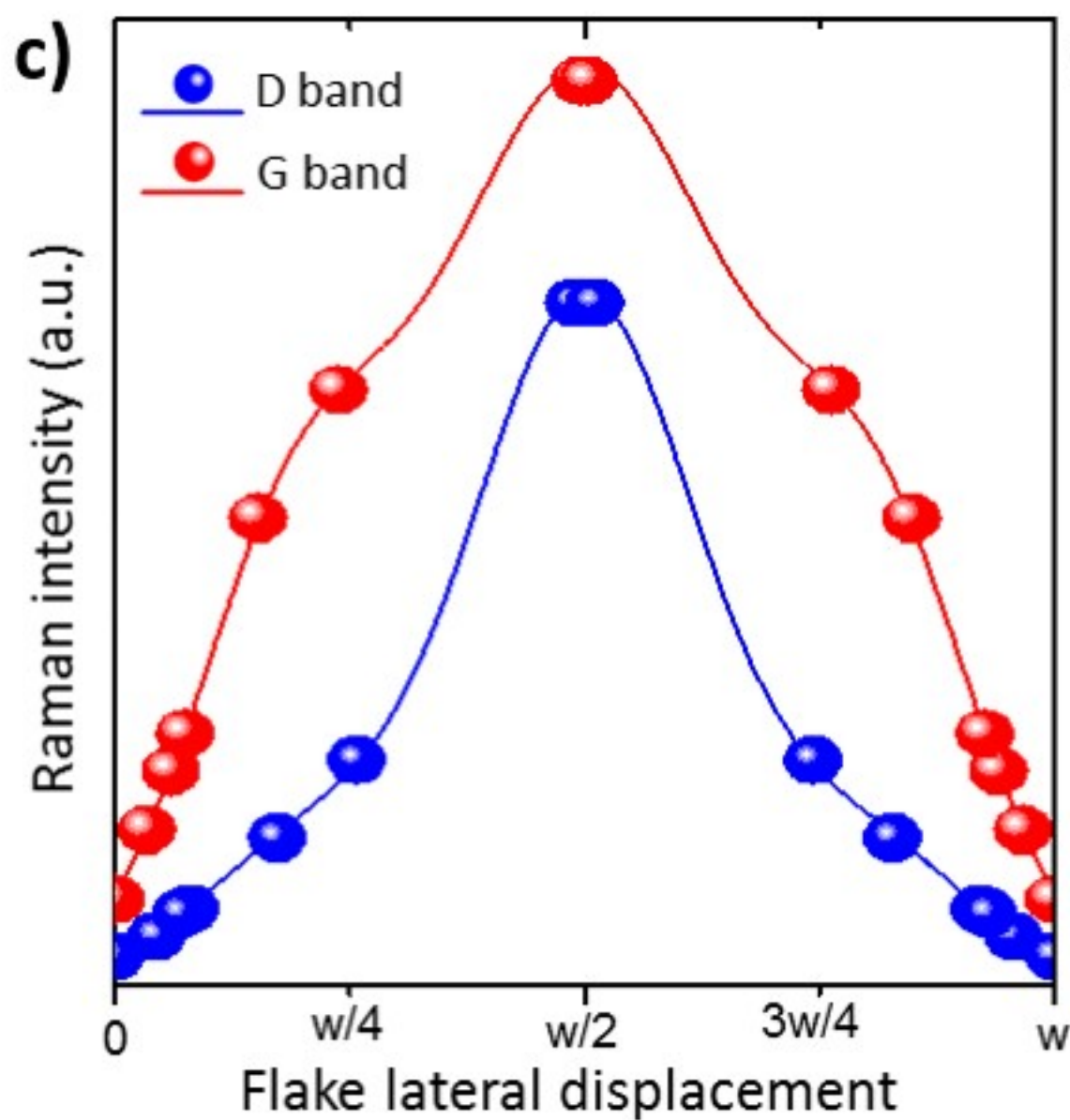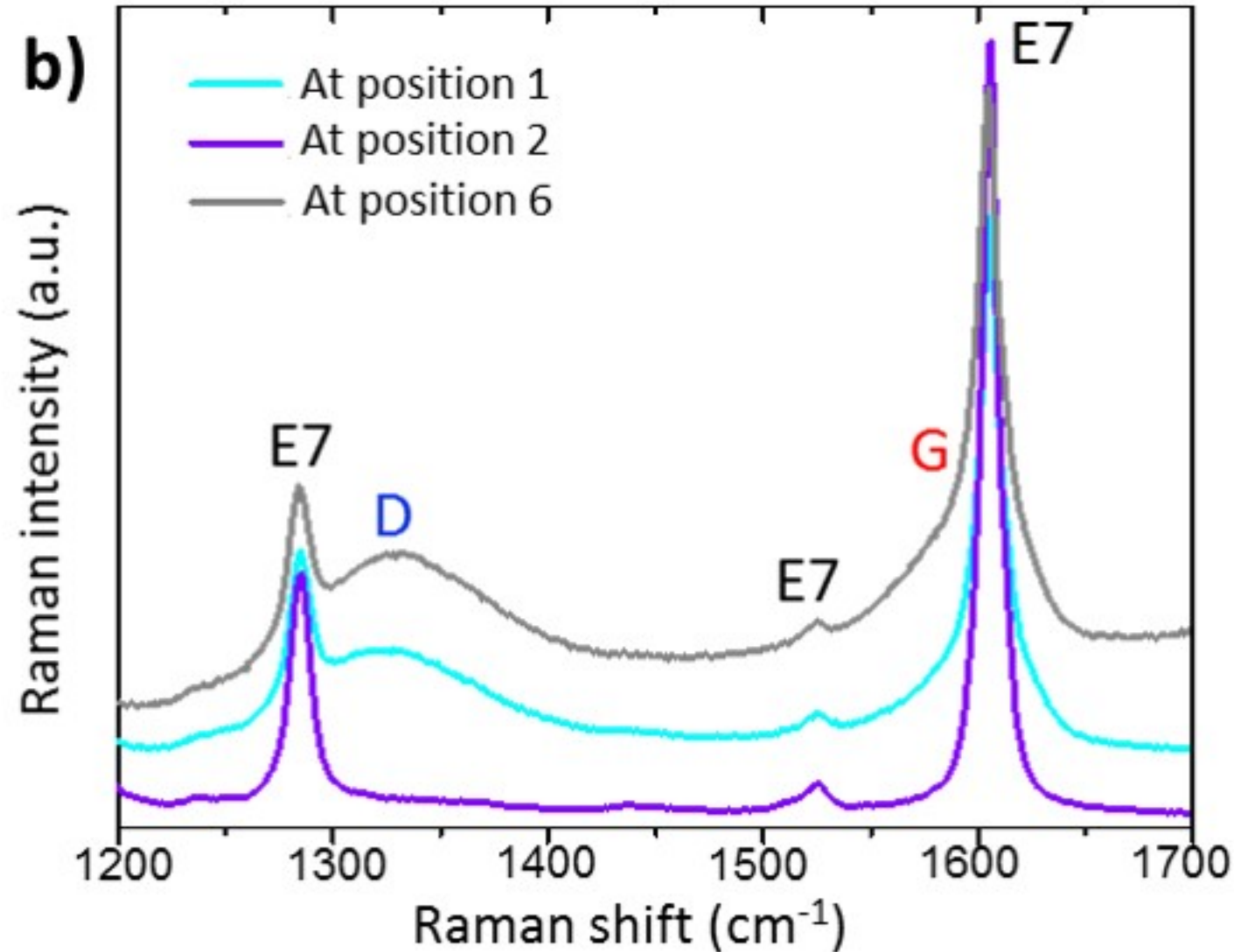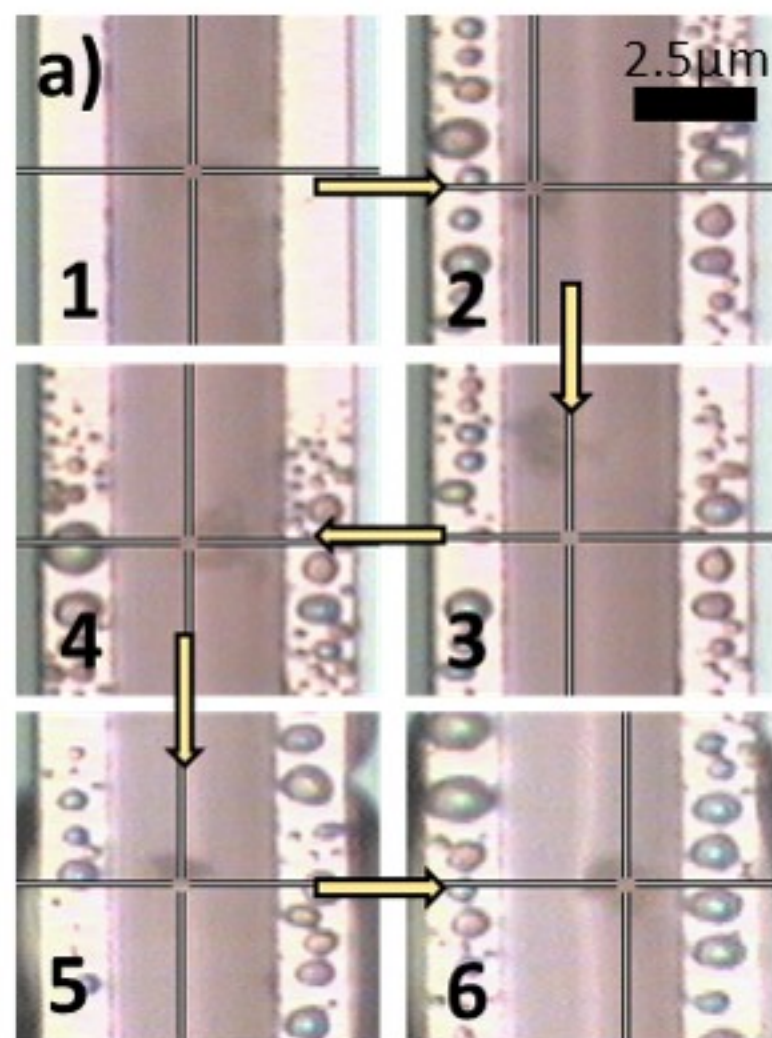
2D Material Metastructures

a) and b) Raman Intensity maps as a function of Optofluidic Waveguide Width (μm) and Buffer Thickness (μm), with Δw and Δh_{BOX} indicated.

a) Si · SiO₂ · Infiltration reservoir · 50μm

b) 50μm

c) GO flake · 3.6μm

d) GO flake · 11.6μm

e) 11.6μm

Dynamic *in-situ* sensing of fluid-dispersed 2D materials integrated on microfluidic Si chip

Benjamin T. Hogan, Sergey A. Dyakov, Lorcan J. Brennan, Salma Younesy, Tatiana S. Perova, Yurii K. Gun'ko, Monica F. Craciun and Anna Baldycheva

Supplementary Methods

Numerical determination of the Raman signal intensity using the scattering matrix method. The scattering matrix method (SMM) is a powerful tool for numerical determination of the near- and far-field light distribution for structures which can be split into layers uniform along at least one direction[1–4]. The main principle of this method is the decomposition of electric and magnetic fields into Fourier series in each layer and connecting the Fourier components of adjacent layers in accordance with the boundary conditions of Maxwell's equations.

In this work, we propose an SOI based optofluidic waveguide channel design (Fig. 1 inset) for in-situ micro-Raman detection and monitoring of integrated 2D fluid nanocomposite. We optimised the optofluidic waveguide design to significantly enhance the back-scattered Raman signal from incorporated 2D nanoplatelets. Raman scattering is a quantum mechanical process with a random spatial distribution of the photons involved, however the optical behaviour of the scattered light can be modelled using a classical electrodynamics approach. 2D flakes within nanocomposites are modelled as a system of chaotically-oriented oscillating electrical dipoles[5] within a microfluidic channel, with the dipole emission defining the Raman signal wavelength. To numerically determine the far-field intensity of the dipole emission the SMM was used.

To reach convergence, 801 Fourier harmonics were used. The local components of the electromagnetic field were found, forming material matrices in each layer. By applying an iterative

procedure, the total scattering matrix for the whole structure was calculated[6]. The back-scattered Raman intensity was calculated from the components of the scattering matrix.

All numerical analyses were made for normal angles of Raman laser incidence and signal collection. The electric field vector of the incident light is oriented parallel to the channel walls. The nematic LC host is a birefringent material, however, an advantage of the microfluidic infiltration into SOI cavities is the spontaneously induced planar alignment of the LC through interaction with the surfaces of the Si walls[7]. The LC will therefore have a director which is either parallel or perpendicular to the walls of the channel such that only either the extraordinary or ordinary refractive index is required.

The spot size of the Raman laser was effectively considered as equal to the microfluidic cavity width. To account for this, all Raman intensities were normalised by accounting for the incident field strength in the channel. Since the incident and Raman-scattered wavelengths of the light are considerably greater than the thickness of 2D flakes in nanocomposites, the flake is considered to be a point dipole- an emitter of only Stokes or anti-Stokes photons within the system- and hence the refractive index of the flake material has no effect on the propagation of backscattered light in the cavity. For Fabry-Pérot effects in a layer to be observed experimentally, its thickness should be less than the coherence length of the Raman scattered light[5]. However, this condition is not fulfilled for the silicon substrate layer, hence it is modelled as a semi-infinite material by removing all Fabry-Pérot resonances within the substrate layer. Very thick silicon walls were considered; the thickness of the silicon walls has been shown to have little effect on the intensities determined by numerical analysis.

Numerical determination of the effect of flake position on the Raman signal intensity. The effect of the flake position on the Raman signal intensity was modelled, using the SMM, by varying the position of the oscillating dipoles within the optofluidic waveguide channel both laterally and vertically. Vertical displacements were defined from the bottom surface of the channel and lateral displacements from a side wall. For vertical displacement variation, the flake was fixed at the lateral

centre while for lateral displacement variation it was fixed at the vertical centre. The liquid crystal in this case was defined as commercially available E7. We chose parameters of the optofluidic waveguide that demonstrate strong enhancement of both the D and G bands.

Calculation of LC refractive indices. The ordinary and extraordinary refractive indices were calculated at all wavelengths subsequently utilised in the numerical analysis by utilising a three-coefficient Cauchy model, $n_{o,e} = A_{o,e} + \frac{B_{o,e}}{\lambda^2} + \frac{C_{o,e}}{\lambda^4}$; where n is the refractive index and A, B and C are suitable fitting parameters. The subscripts o and e represent the ordinary and extraordinary indices respectively. For example, for commercially available LC MLC 6608, A_o, B_o and C_o were set to 1.4609, 5×10^{-3} μm^2 and 0 μm^4 respectively to give good agreement with experimental measurements in the visible region[8]. As MLC 6608 has a low birefringence in the visible region, the two-coefficient Cauchy model is a sufficient approximation.

Synthesis of GO-LC nanocomposites. Graphene oxide (GO) was prepared from bulk graphite *via* the Hummers method[9]. 1 g of graphite, 0.5 g of sodium nitrate and 23 mL of sulfuric acid (H_2SO_4) were added to a 500 mL round bottomed flask contained within an ice bath and stirred at 4 $°C$ for 15 minutes. 3 g of potassium permanganate ($KMnO_4$) was added slowly with vigorous stirring. Once all the $KMnO_4$ was added, the ice bath was removed and the suspension was heated to 35 $°C$ for 30 minutes. This produced a murky brownish-grey solution. Following this, 46 mL of water was added and the suspension was set to stir for 15 minutes. The solution was then treated with 1.4 mL of hydrogen peroxide (H_2O_2). The product was washed through centrifugation up to 10 times with a 10 % aqueous solution of hydrochloric acid (HCl) followed by copious amounts of deionised water. The resulting GO was suspended in H_2O and filtered under vacuum onto an omniporous 200 nm membrane, washed with 1 L of H_2O and then dried at 80 $°C$ for several days. Once dried, the GO was dispersed in tetrahydrofuran (THF) through ultrasonication, exfoliating the material down to a few layers[10]. The dispersions were then centrifuged, allowing for extraction of the lowest mass GO flakes from the top layer of the suspension. An aliquot from this layer was mixed with the liquid crystal and

the mixture underwent further ultrasonication to ensure thorough mixing of the two components. The resulting dispersion was dried in a Schlenk flask, under vacuum, allowing for complete evaporation of the residual solvent, resulting in a nanocomposite of GO nanoplatelets uniformly dispersed in the liquid crystal. The concentration of GO in the final nanocomposites was approximately 0.01 $g.ml^{-1}$. Dispersed flakes had average sizes of around 1 μm^2 and were typically found to be between 1 and 5 layers thick. The number density of graphene oxide particles was calculated to be approximately 10^{12} *particles/ mL*. Graphene nanocomposites were produced by a similar method starting from bulk graphite powder.

Instrumentation. Scanning electron microscopy (SEM) measurements were performed on a Hitachi S3200N system with a practical operational magnification between 20-60000x, accelerating voltages from 0.3 to 30 *kV*, vacuum chamber pressure <0.1 *mbar* and a maximum resolution of 3.5 *nm*. Micro-Raman measurements were performed using a Renishaw 1000 system (with a 514.5 nm excitation wavelength from Ar^+ laser, a power of 5 *mW* and a spot size of approximately 3 μm) and on a Horiba Raman system (with an excitation wavelength of 532 *nm*, a power of 8.75 *mW* and a spot size of approximately 5 μm when focused through a x50 objective). Polarised light images were obtained using a Zeiss Axioscope 2 microscope with a Zeiss Axiocam MRc 5 camera, with x20 and x50 objectives used.

Supplementary Results

Raman intensity maps. Maps were produced separately for the D and G bands of 2D carbon-based materials such as graphene or GO (Sup. Fig. 1). Strong variations in the Raman intensity are observed as various parameters of the optofluidic waveguide are varied.
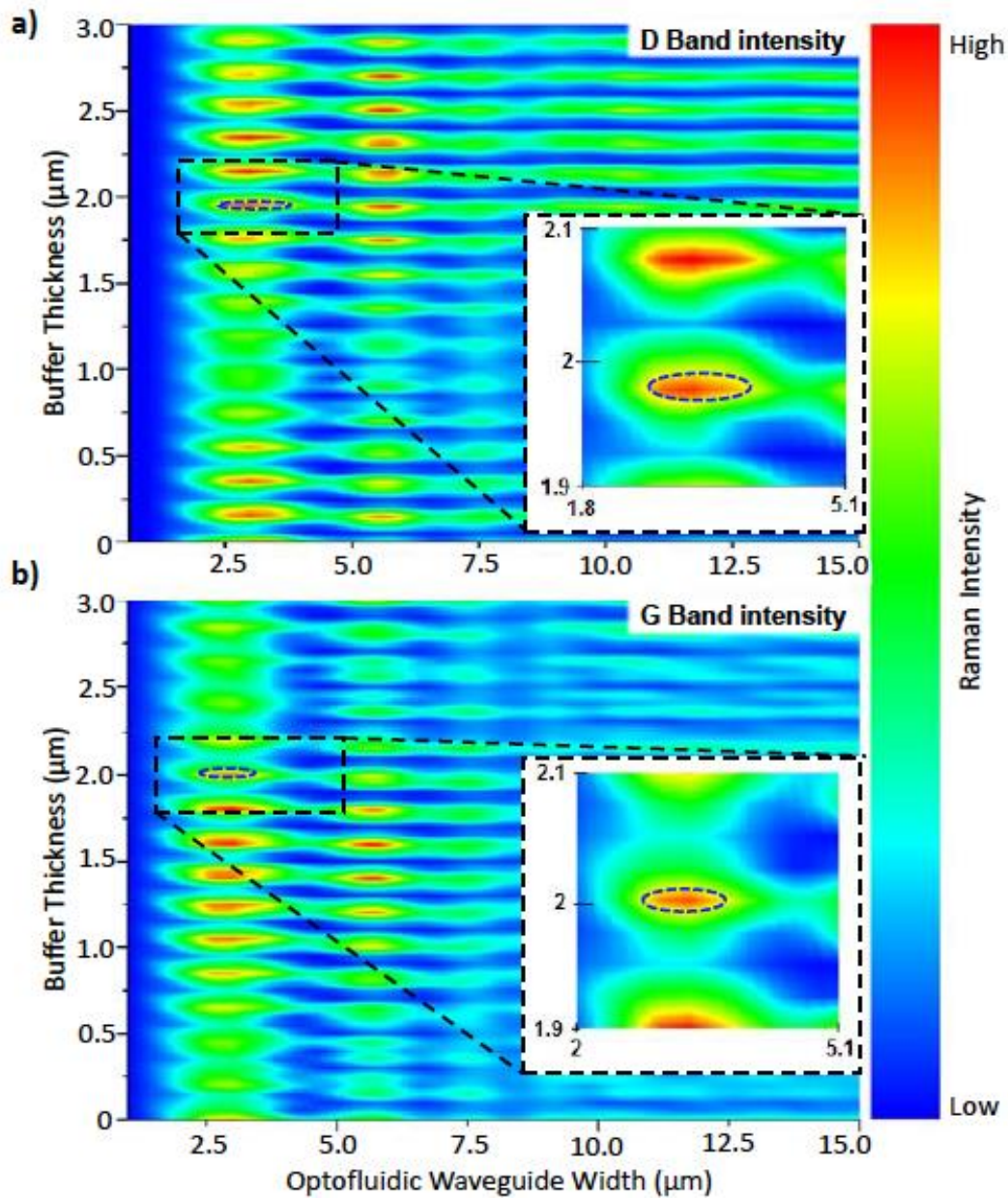
Supplementary figure 1: Maps of the Raman signal intensity at wavelengths corresponding to **a**) the D band and **b**) the G band of fluid-dispersed 2D carbon-based materials, under excitation by a 532nm Raman laser, as the optofluidic waveguide width and buffer oxide layer thicknesses are varied. High intensity areas of interest are highlighted.

Liquid crystal spectra. The liquid crystal host materials used for the nanocomposites in experimental measurements have several characteristic bands in their Raman spectra (Sup. Fig. 2) which are then also present in the spectra of the nanocomposites. The spectra were recorded for droplets of the liquid crystal greater than 100 μm deep, on a SOI substrate. The spectrum for MLC 6608 has been scaled by a factor of four. E7 shows a strong Raman active vibrational band at around 1605 cm^{-1}, overlapping with the G band of graphene oxide. There is an additional strong band at around 1280 cm^{-1}, which partially overlaps with the D band of graphene oxide, as well as two very weak bands at around 1440 cm^{-1} and 1525 cm^{-1}. MLC 6608, however, only shows weak bands at around 1245 cm^{-1}, 1305 cm^{-1}, 1355 cm^{-1}, 1450 cm^{-1}, 1460 cm^{-1} and 1640 cm^{-1}.
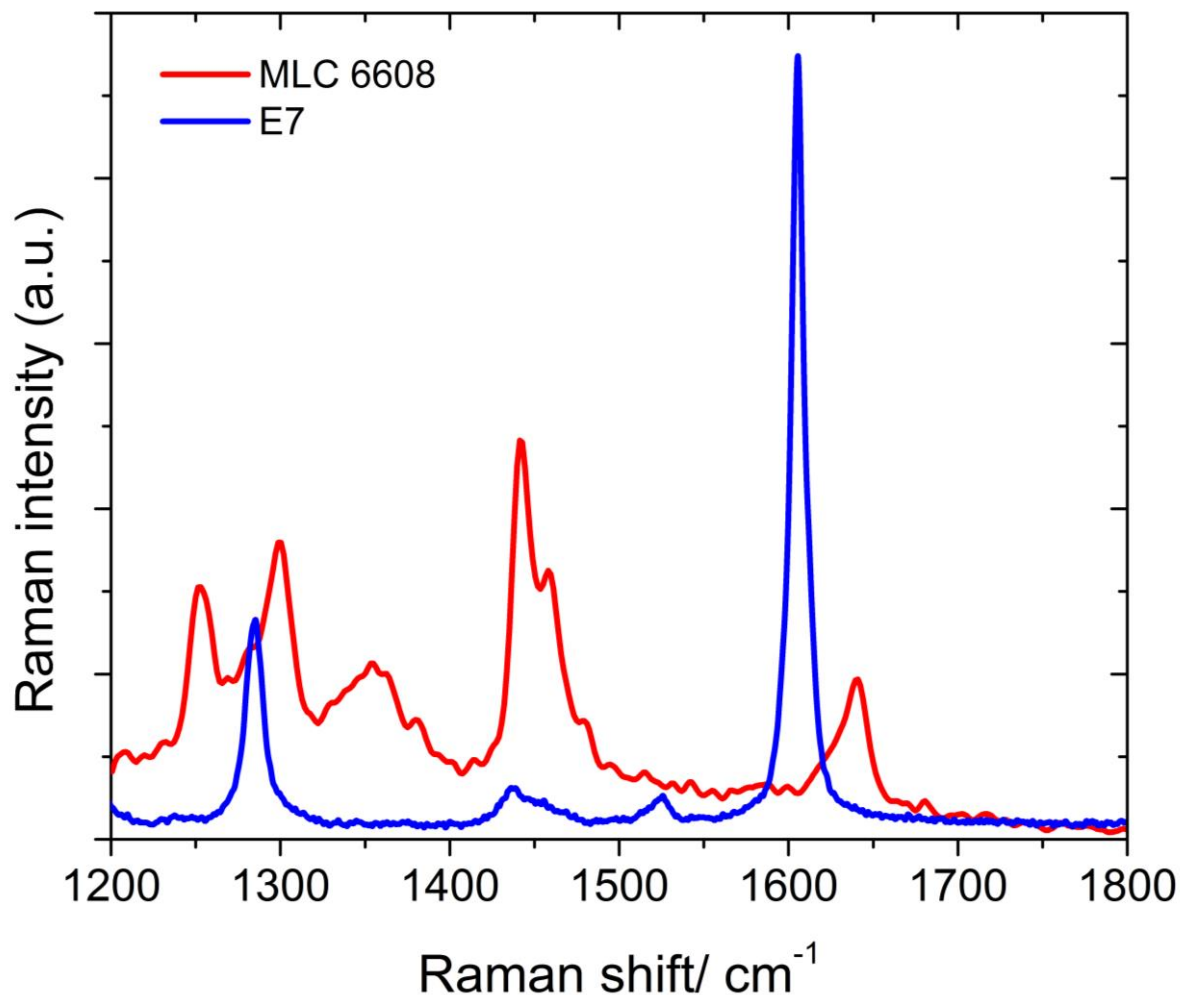
Supplementary figure 2: Raman spectra for droplets of the liquid crystal host fluids used in the synthesised nanocomposites on a SOI substrate: MLC 6608 (red) and E7 (blue). The spectrum for MLC 6608 has been scaled by a factor of four.

Nanoparticle alignment by external stimuli. The GO flakes dispersed in the LC can be manipulated by re-orienting the LC director (See Sup. Vid. 1). Applying an electric field across the channel results in a switching of the orientation of the LC molecules when a threshold voltage between the two walls is reached[11,12] (See Sup. Vids. 2-3). This is observed as a change from a bright to a dark state in polarised optical microscopy. For the GO dispersion in LC E7, an off-chip threshold voltage of approximately 3.5 *V* was observed in a 50 μm wide channel (Sup. Fig. 3). As the voltage was increased further above the threshold voltage, bands of light and dark states appeared, with the light state bands centred around GO flakes positioned next to the channel walls. Smaller flakes in the centre of the channel are observed to move as the voltage is increased.
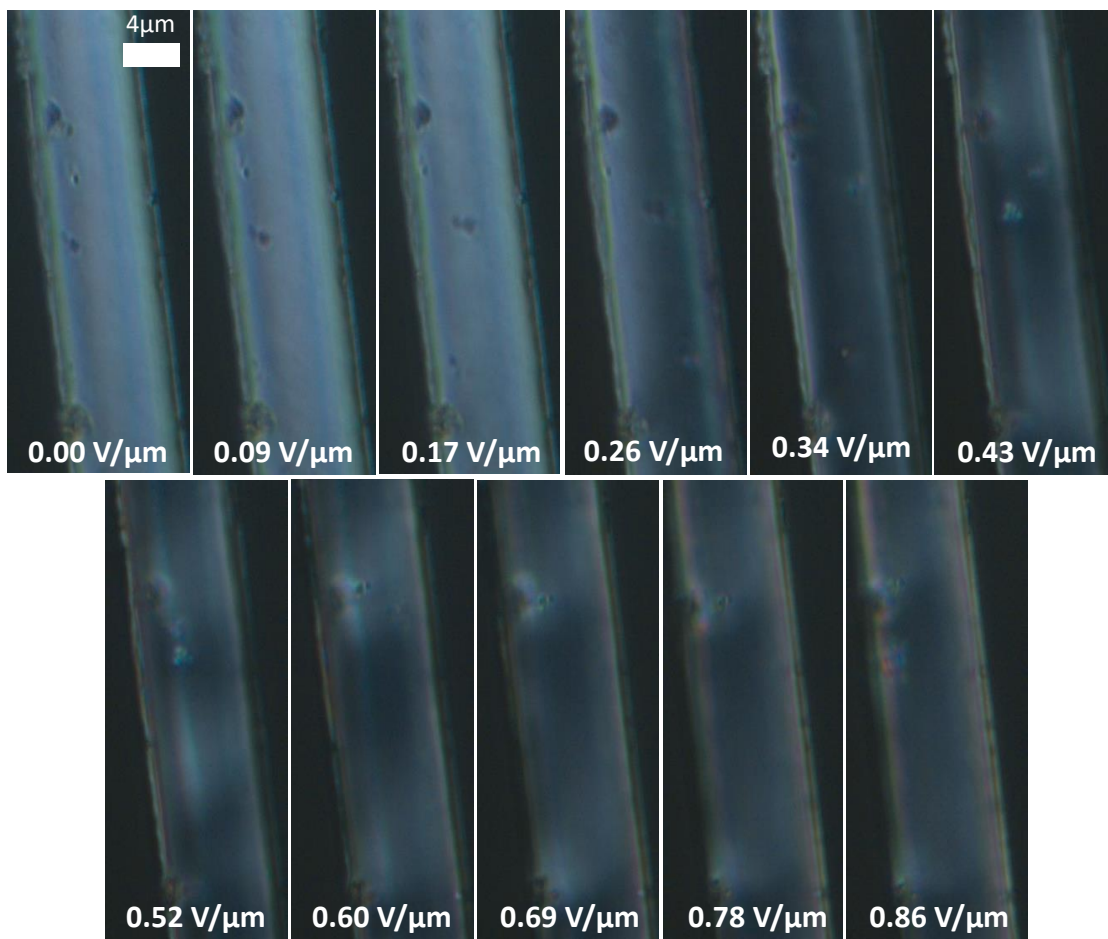
Supplementary figure 3: Polarized optical microscopy images showing the change in orientation of liquid crystal E7, with GO flakes dispersed, as the applied field strength between the walls of an 11.6 μm wide channel is increased.

The Raman laser can also be used to induce repositioning and reorientation of the dispersed flakes[13]. Flakes can be induced to rise within the fluid host or to move towards (or away from) the walls of the channel controllably. Flake movement can be observed as strong changes in the

interference pattern observed in the back-scattered light. In particular, flakes were shown to be drawn towards the laser spot and to circle the centre of the spot (See Sup. Vid. 4) when the laser intensity was suitably high. This allowed controllable repositioning of the flakes within the microfluidic channels.

In-situ *detection of nanoparticle positions.* The positions of the individual GO flakes within the liquid crystal host can be accurately predicted from the Raman spectra, specifically by looking at the G and D band intensities relative to a reference position. Supplementary Table 1 summarises the predicted positions shown in Fig. 5c of the main text. For each of the six experimental positions determined, there was a strong agreement between the predictions made using the D and G band intensities respectively, with the greatest disparity being just 2 *%* of the optofluidic waveguide width.

Supplementary table 1: Summary of positions predicted for various flake alignments by comparing to reference data (*) normalised relative to numerically determined values.

Flake designation	Normalised D band intensity (a.u.)	Position corresponding to D band intensity (% of cavity width)	Normalised G band intensity (a.u.)	Position corresponding to G band intensity (% of cavity width)	Difference between D and G positions (% of cavity width)
Ref*	0.05*	0.000 / 1.000	0.18*	0.000 / 1.000	0.0000
A	0.09597	0.045 / 0.955	0.33937	0.034 / 0.966	1.1000
B	0.14839	0.071 / 0.929	0.47437	0.060 / 0.940	1.1000
C	0.15806	0.081 / 0.920	0.56063	0.075 / 0.925	0.5500
D	0.32177	0.173 / 0.827	1.05563	0.153 / 0.847	2.0000
E	0.5	0.258 / 0.742	1.35	0.238 / 0.762	1.9230
F	1.55	0.489 / 0.511	2.06	0.496 / 0.504	0.7000

For each experimental flake position, there are two predicted values given for the D and G peaks respectively. This is due to centrosymmetric nature of the cavity in the *x* direction. By breaking this symmetry- for example by using an off-centre laser spot or by having walls of different permittivity-

the numerical analysis would no longer return a centrosymmetric intensity profile which may lead to a single position being determinable.

For flake position A, optical microscopy determined that the flake was aligned precisely next to the wall of the optofluidic waveguide. The position as determined from the Raman spectrum suggested the flake was displaced by around 4.5 *%* if looking at the D band or 3.4 *%* if looking at the G band. Similarly, for flake position E, optical microscopy determined that the flake was positioned 21 *%* of the way across the channel. The position as determined from the Raman spectrum suggested the flake was displaced by around 25.8 *%* if looking at the D band or 23.8 *%* if looking at the G band. For flake position F, optical microscopy determined that the flake was positioned 45 *%* of the way across the channel. The position as determined from the Raman spectrum suggested the flake was displaced by around 48.9 *%* if looking at the D band or 49.6 *%* if looking at the G band. In all cases, the position predicted from both the D and G bands individually was within a few *%* of the optical microscopy measurement. It was estimated that the optical microscopy measurements had an error of approximately ±5 *%* due to the difficulty in accurately observing the flake edges and hence the centre of the flake.

Supplementary References

1.   Dyakov, S. A. *et al.* Surface states in the optical spectra of two-dimensional photonic crystals with various surface terminations. *Phys. Rev. B* **86,** 115126 (2012).

2.   Christ, A., Tikhodeev, S. G., Gippius, N. A., Kuhl, J. & Giessen, H. Waveguide-Plasmon Polaritons: Strong Coupling of Photonic and Electronic Resonances in a Metallic Photonic Crystal Slab. *Phys. Rev. Lett.* **91,** 183901 (2003).

3.   Tikhodeev, S. G., Yablonskii, A. L., Muljarov, E. A., Gippius, N. A. & Ishihara, T. Quasiguided modes and optical properties of photonic crystal slabs. *Phys. Rev. B* **66,** 045102 (2002).

4.   Dyakov, S. A. *et al.* Influence of the buffer layer properties on the intensity of Raman scattering of graphene. *J. Raman Spectrosc.* **44,** 803–809 (2013).

5.   Dyakov, S. A. *et al.* Optical properties of grooved silicon microstructures: Theory and experiment. *J. Exp. Theor. Phys.* **113,** 80–85 (2011).

6.   Ko, D. Y. K. & Inkson, J. C. Matrix method for tunneling in heterostructures: Resonant tunneling in multilayer systems. *Phys. Rev. B* **38,** 9945–9951 (1988).

7.   Sengupta, A., Herminghaus, S. & Bahr, C. Liquid crystal microfluidics: surface, elastic and viscous interactions at microscales. *Liq. Cryst. Rev.* **2,** 73–110 (2014).

8.   Li, J., Wen, C.-H., Gauza, S., Lu, R. & Wu, S.-T. Refractive Indices of Liquid Crystals for Display Applications. *J. Disp. Technol.* **1,** 51–61 (2005).

9.   Hummers, W. S. & Offeman, R. E. Preparation of Graphitic Oxide. *J. Am. Chem. Soc.* **80,** 1339–1339 (1958).

10.   Paredes, J. I., Villar-Rodil, S., Martínez-Alonso, A. & Tascón, J. M. D. Graphene Oxide Dispersions in Organic Solvents. *Langmuir* **24,** 10560–10564 (2008).

11.   Tie, W. *et al.* Dynamic electro-optic response of graphene/graphitic flakes in nematic liquid crystals. *Opt. Express* **21,** 19867–79 (2013).

12.   Shen, T.-Z., Hong, S.-H. & Song, J.-K. Electro-optical switching of graphene oxide liquid crystals with an extremely large Kerr coefficient. *Nat. Mater.* **13,** 394–9 (2014).

13.   Twombly, C. W., Evans, J. S. & Smalyukh, I. I. Optical manipulation of self-aligned graphene flakes in liquid crystals. *Opt. Express* **21,** 1324–34 (2013).

Supplementary Video Captions

Supplementary video 1: Orientation switching of a graphene flake, dispersed in E7, in a 50 μm diameter microfluidic reservoir. A pulsed electrical field is applied and a corresponding change in the flake alignment and patterning of the LC surface are observed. The video was taken using cross-polarised light.

Supplementary video 2: Induced motion of GO flakes, dispersed in E7, in an 11.6 μm wide channel. A bias is applied across the channel and is steadily increased. Switching of the LC director occurs above a threshold applied field strength of 0.25 $V/\mu m$. As the LC director is switched, motion of the dispersed GO flakes is observed. The video was taken with cross-polarised light.

Supplementary video 3: Induced motion of a single GO flake, dispersed in MLC-6608, in an 11.6 μm wide channel. An electric field is applied across the channel and is increased and decreased periodically above and below the threshold applied field strength. Induced rotational and translational motion of the flake is observed. The video was taken using unpolarised light.

Supplementary video 4: Optically induced motion of GO flakes, dispersed in MLC-6608, in a 50 μm diameter microfluidic reservoir is observed. Motion can be seen as a change in the interference

pattern of the backscattered light from the Raman laser. Optical trapping with particles drawn to high light intensity regions is observed.